JOURNAL OF GEOPHYSICAL RESEARCH, VOL. 112, C06022, doi:10.1029/2006JC003625, 2007

A surface velocity spiral observed with ADCP and HF radar in the Tsushima Strait

Y. Yoshikawa,[1] T. Matsuno,[1] K. Marubayashi,[1] and K. Fukudome[2]

Received 6 April 2006; revised 2 February 2007; accepted 12 March 2007; published 26 June 2007.

[1] The structure of a wind-driven flow in the Tsushima Strait is investigated with moored acoustic Doppler current profiler (ADCP) and HF radar. Two ADCPs of high and low acoustic frequencies are simultaneously used to measure velocities in both the surface boundary layer and the interior with high resolutions. The velocity relative to an interior flow in the surface boundary layer is estimated by subtracting the reference velocity (estimated from velocities at greater depths) from a velocity in the surface layer, and complex principal component analysis (PCA) of the lagged wind stress and the relative velocity is performed. Despite a short (2 weeks) observation period of relatively calm and variable wind, a clockwise velocity spiral similar to a theoretical Ekman spiral is detected as the first mode of PCA. Ekman transport estimated from the relative velocities of the first mode agrees best with Ekman transport expected from wind stress of the first mode with 11–13 hours time lag, for which the explained variance of the first mode is also largest. This indicates that a wind-driven flow is balanced with wind stress after 11–13 hours, half of the inertial period at this latitude. Eddy viscosity is also inferred from wind stress and the relative velocities of the first mode. It is found to increase from $O(10^{-3})$ m^2 s^{-1} at greater depth to $O(10^{-2})$ m^2 s^{-1} near the sea surface.

Citation: Yoshikawa, Y., T. Matsuno, K. Marubayashi, and K. Fukudome (2007), A surface velocity spiral observed with ADCP and HF radar in the Tsushima Strait, *J. Geophys. Res.*, *112*, C06022, doi:10.1029/2006JC003625.

1. Introduction

[2] Wind over the Tsushima Strait (Figure 1) is occasionally high in summer and always strong in winter. A surface boundary flow driven by local wind stress (hereafter referred to as a wind-driven flow) is thus expected to be occasionally large in summer and always intense in winter. HF radar deployed in this strait [*Yoshikawa et al.*, 2006] measures a surface current comprising a shallow wind-driven flow and interior flows such as a geostrophic current (the Tsushima Warm Current) and tidal currents. To estimate an interior flow field from HF radar measurement, the wind-driven velocity must be separated from a total velocity measured with HF radar.

[3] According to the classical linear theory of *Ekman* [1905], a steady wind-driven velocity spirals clockwise with depth in the Northern Hemisphere. Several field studies [*Weller*, 1981; *Price et al.*, 1986; *Stacey et al.*, 1986; *Richman et al.*, 1987; *Weller et al.*, 1991; *Wijffels et al.*, 1994; *Chereskin*, 1995; *Lee and Eriksen*, 1996; *Schudlich and Price*, 1998] found similar velocity spirals in the actual ocean. However, some spirals were flatter than the Ekman spiral; current rotated less with depth than Ekman theory. *Price et al.* [1986] showed that diurnal variations of stratification and eddy viscosity make a velocity spiral flatter as observed. This demonstrates the crucial importance of eddy viscosity on a detailed structure (spiral) of a wind-driven flow. However, our knowledge of in situ eddy viscosity is very limited. This means that a structure of wind-driven flow in the Tsushima Strait cannot be accurately predicted. Thus the structure needs to be measured and identified.

[4] There are many difficulties in measuring a wind-driven flow in the Tsushima Strait. Very active fisheries and marine traffic in this strait make a long-period surface mooring impractical although it is desirable for accurate measurement of a wind-driven flow [e.g., *Schudlich and Price*, 1998]. Access to the mooring site should be kept available during our field observation period in case of an unexpected accident between a moored buoy and ships or boats. This and the limited ability of our small ship do not allow operations in winter during large wave heights caused by strong northwesterly monsoon wind. Thus a wind-driven flow has to be measured in summer, a season of calm and variable wind.

[5] Our observation period spanned for 2 weeks, from 5 to 21 July 2005. To measure a wind-driven flow within a limited period with good accuracy, two acoustic Doppler current profilers (ADCPs) of different acoustic frequencies were moored at the surface in an HF radar measurement area. Principal component analysis (PCA) was performed to detect the wind-driven flow component covarying with wind stress. The velocity spiral corresponding to a theoretical Ekman spiral was obtained as the first mode of PCA. In section 2, an

[1] Research Institute for Applied Mechanics, Kyushu University, Fukuoka, Japan.
[2] Interdisciplinary Graduate School of Engineering Sciences, Kyushu University, Fukuoka, Japan.

0148-0227/07/2006JC003625$09.00

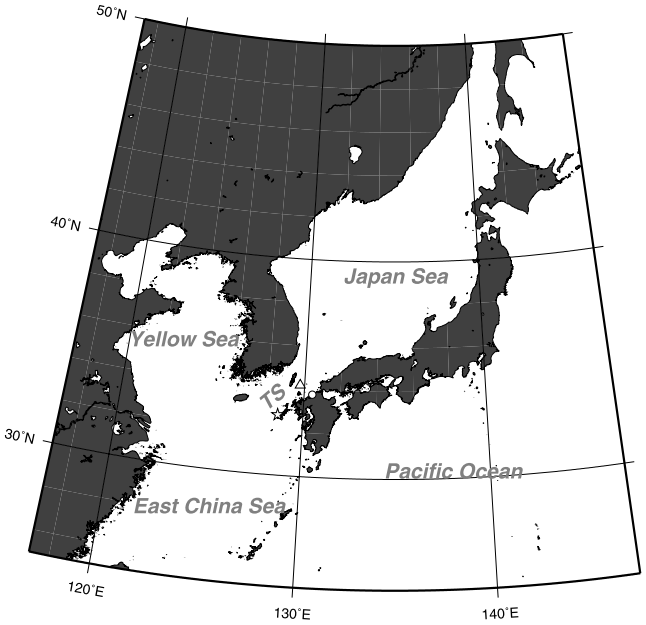

Figure 1. Location of the Tsushima Strait (TS). Mooring site (open triangle), JMA wave height station (Fukuejima; open star), and marine tower station (Tsuyazaki; open circle) are also indicated.

outline of our field measurement and data source is described. Expected errors of current velocity and wind stress are shown in section 3. Wind, current, and temperature data are shown in section 4, and the wind-driven flow detected from PCA is presented in section 5. A component other than the wind-driven flow and a profile of vertical eddy viscosity inferred from the wind-driven flow are discussed in section 6. Finally, concluding remarks are given in section 7.

2. Field Observation and Data Source

2.1. Surface Moored Buoy

[6] A surface moored buoy as illustrated in Figure 2 was deployed on 5 July 2005 by T/V Nagasaki-Maru of Nagasaki University. The buoy is anchored at about (34.175°N, 129.75°E) in an HF radar measurement area with a 250-m rope where the total water depth is about 100 m (Figure 3). For unexpected drifting of the buoy due to an accident, the buoy position was tracked every hour by GPS and was sent to laboratory's PC via e-mail using ORBCOMM system.

[7] Motion of the buoy is affected by both currents and surface waves. Figure 4 shows time series of averaged pitch (tilt in the direction of the flow) and roll (tilt in the direction transverse to the flow) of moored ADCP (averaging interval is 10 min). Diurnal and semidiurnal oscillations as well as higher-frequency oscillations are evident. The former oscillations are more evident in pitch record, indicating that stronger tidal current periodically pushed and tilted the moored buoy to a greater degree. The latter oscillations are due to surface waves. Note that instantaneous pitch and roll are expected much larger than averaged ones shown in Figure 4. Surface waves not only stir the platform to increase measurement error but also induce large orbital velocity, which acts as noise for our measurement of a wind-driven flow. Thus surface waves infect ADCP measurement, though they are not a major problem in the present analysis, as described in later sections.

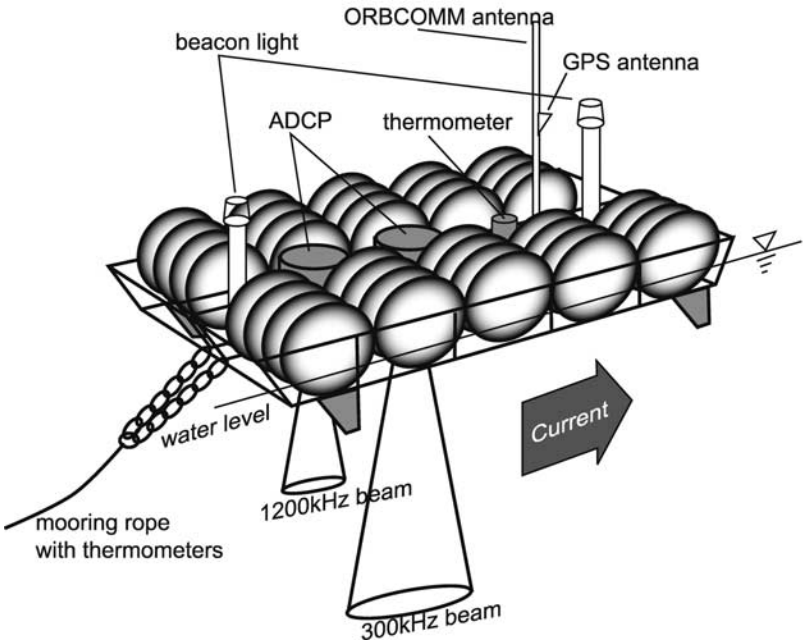

Figure 2. Schematic illustration of a moored surface buoy. A buoy is composed of 10 dram-shaped floats, frame of 2.58 m in length and 1.87 m in width, two ADCPs, thermometer, ORBCOMM and GPS system, and beacon lights. Transducers of ADCP are set below the level of drum-shaped float's bottom and about 0.3 m below water level.

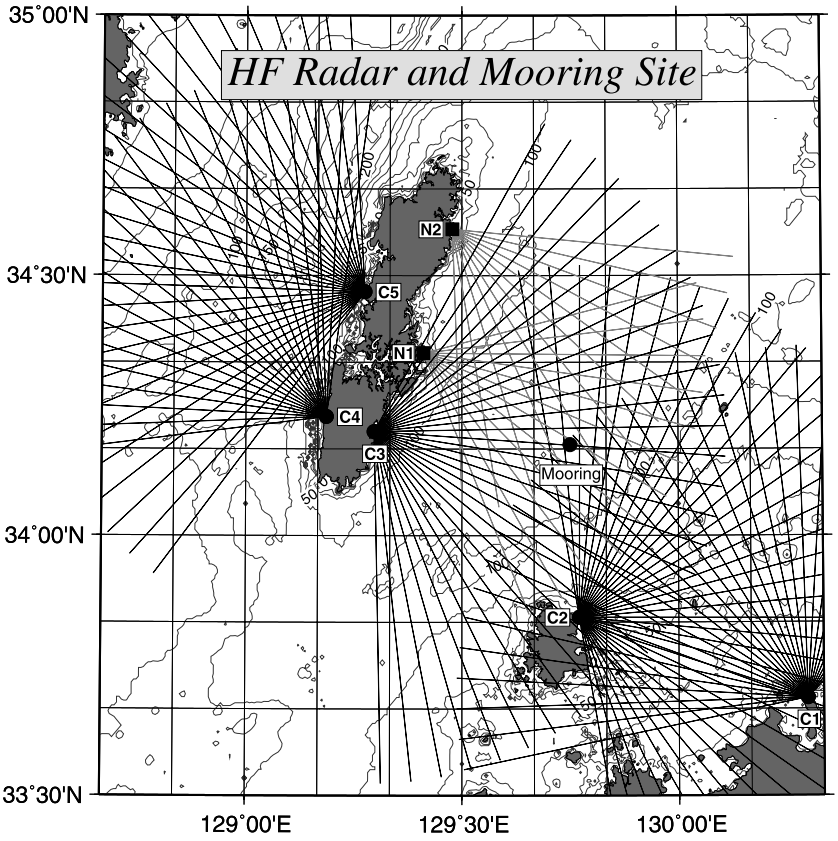

Figure 3. Location of mooring site and HF radar sites (CODAR: C1–C5, NJRC: N1 and N2). Looking lines and range coverage of each radar are drawn by lines.

2.2. Velocity Data

2.2.1. ADCP

[8] To increase vertical resolution of velocity measurement in both the surface boundary layer and the interior, we equipped a moored buoy with two ADCPs (RDI 300 kHz/1200 kHz). The 300-kHz ADCP measures velocities from 6 m depth to the bottom with 4 m depth interval in bottom-tracking mode, while the 1200-kHz ADCP measures velocities from 0.4 to 8.0 m depth with 0.2-m-depth interval. The 300-kHz ADCP mainly measures an interior flow at greater depths. In order to estimate a wind-driven flow, the interior flow is extrapolated to shallower depths and is subtracted from a total flow in the surface boundary layer measured by the 1200-kHz ADCP. The two ADCPs are synchronized with each other; the 1200-kHz ADCP transmits acoustic signal 1 s after the 300-kHz ADCP transmits. The synchronization scheme did not operate with burst mode of pinging, which would effectively reduce aliasing of orbital velocity into ADCP velocity. Thus both ADCPs are set to transmit signals every 10 s and record a velocity every 10 min (60-ensemble average). This sampling interval permits the orbital velocities of $10/n$ s wave period ($n = 1, 2, \ldots$) to be perfectly aliased into ADCP velocity. The magnitudes of these orbital velocities are estimated from wave height (section 4). To minimize measurement error due to platform motion caused by surface waves, we applied to the 300-kHz ADCP the mode which allows the ADCP to collect both water profile data and bottom-track data from single ping (this mode is included in LADCP feature.) The ADCP velocity is averaged every hour (for example, 00:30–01:30 average for hourly velocity at 01:00) to obtain hourly ADCP velocity.

[9] The bottom-track velocity measured by the 300-kHz ADCP was found to be biased. The velocity indicates a long (10 km) drift of moored buoy for 2 weeks although GPS data do not show the longer drift than is allowed by a mooring rope. Part of this error seems to be aliasing error due to platform motions caused by surface waves (described in later section), and other part seems to be related to a limited bottom-tracking ability of the mode which collects both water profile and bottom-track data simultaneously. Although this error was small ($\leq$1.0 cm s^{-1} = 10 km/2 weeks), the velocity estimated from hourly GPS data of the buoy was used as the bottom-track velocity (note that this does not affect the estimation of a wind-driven velocity). A bias error is also found in a velocity measured by the 1200-kHz ADCP near the sea surface. The velocity magnitude above about 2 m depth was always smaller than the velocity below. This feature is independent of wind magnitude and direction. Therefore we consider that this bias is related to the structure of mooring system itself which disturbed flow field near the surface. For this reason, velocity below 2.5 m depth is used in this study. Variance of error velocities of the 1200-kHz ADCP is found to be larger than that of the 300-kHz ADCP. To increase statistical accuracy of the 1200-kHz ADCP, the velocity measured by the 1200-kHz ADCP is averaged over 1 m bin. Velocity measured by the 300-kHz ADCP at 6 m is not

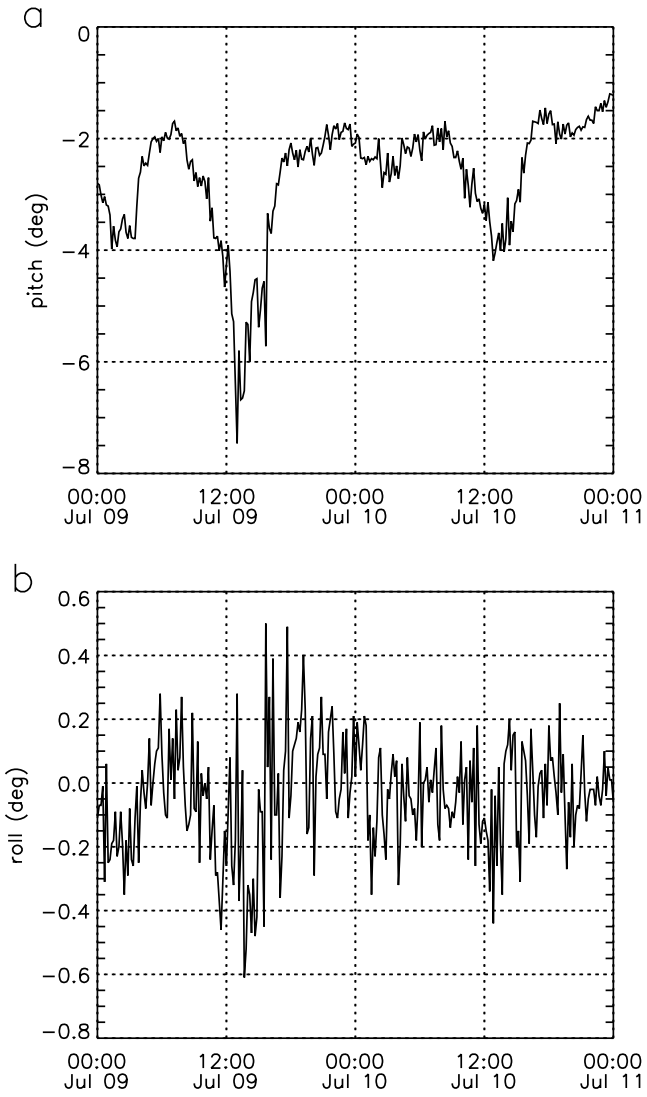

Figure 4. Time series of averaged (a) pitch and (b) roll of moored ADCP. Averaging interval is 10 min. Note the difference in vertical scale between Figures 4a and 4b.

used because its error velocity was exceptionally large. In summary, ADCP velocities used in this study are at 3 to 8 m with 1 m bin size and at 10 m to the bottom with 4 m bin size.

2.2.2. HF Radar

[10] Two types of HF radar, cross-looped antenna type (CODAR; C1–C5) and array antenna type with DBF technique (NJRC; N1–N2), are installed in the Tsushima Strait (Figure 3). CODAR and NJRC radars transmit 13.9 and 24.5 MHz signals to measure an averaged velocity over about 1.72- and 0.98-m-depth ranges, respectively. A total of five radars (C1–C3 and N1–N2) measured surface current at the mooring site. However, comparison with ADCP velocity indicates large measurement errors of C1 and C3 radars (section 3). For this reason, only N1 and N2 (NJRC) radars are used in this study. NJRC is scheduled to transmit signal for 30 min every hour (N1: 44–14 min, N2: 46–16 min) and estimates a 30-min averaged velocity that is used as an hourly HF radar velocity. Further details of specification of HF radars in the Tsushima Strait are described in the paper of *Yoshikawa et al.* [2006].

2.2.3. Velocity Data Set

[11] Hourly velocity data set used in this study is obtained by simply combining hourly ADCP velocities below 3 m depth and hourly HF radar velocity at 0.5 m depth. Velocity is thus obtained at 0.5 m depth with 1 m bin size (HF radar), from 3 to 8 m depth with 1 m bin size (the 1200-kHz ADCP) and from 10 m depth to the bottom with 4 m bin size (the 300-kHz ADCP). To remove high-frequency current variation (such as tidal currents) from velocity data, a low-pass filter (25 hours running mean) is applied to hourly velocity data. In the following analysis, these smoothed hourly velocity data are used.

2.3. Temperature

[12] To measure upper stratification which may affect on the structure of a wind-driven flow [*Price et al.*, 1986], thermometers were attached with a moored buoy at the sea surface and along a mooring rope at 5, 10, and 30 m distant from the surface (water density is mainly determined by temperature in the observation area). Unfortunately, the deepest thermometer did not operate appropriately. In the present analysis, temperatures measured by upper three thermometers sampled every hour are used.

2.4. Wind Stress

[13] Our buoy was designed to be as light as possible in order to measure a velocity near the sea surface. Thus an anemometer was not attached. Instead, reanalyzed surface wind data published by Japan Meteorological Agency (JMA) every 6 hours with 0.125° (longitude) × 0.1° (latitude) resolution (GPV-MSM data) are used in this study. Surface wind stress is estimated from these wind data with drag coefficient formula of *Yelland and Taylor* [1996]. Although *Yelland and Taylor* [1996] formulated the drag coefficient for wind higher than 3 m s^{-1}, we applied the formula even when the wind speed is lower than 3 m s^{-1}.

2.5. Wave Height of Surface Waves

[14] Surface wave height was not measured at the mooring site. Instead, it is estimated from wave height measured by JMA at Fukuejima (Figure 1). This station is to the southwest of our mooring site and is the closest (190 km) station among the available stations during our field observation. The wave height is measured for 20 min (35–55 min) every hour with 0.25 s interval.

3. Error Estimation

3.1. Variance Error of ADCP Velocity

[15] A variance error of ADCP velocity is first estimated by comparing the 300-kHz ADCP velocity at 10 m and the 1200-kHz ADCP velocity at 8 m (note that a bias error of ADCP velocity is not fully estimated from this comparison because the error might be cancelled when comparing two ADCP velocities). Table 1 shows regression coefficients, correlation, and root mean square (RMS) difference from the regression line. Small RMS (1.52 cm s^{-1}) between two velocities suggests the small variance error of ADCP measurement itself. Difference between the bottom-track velocity measured by the 300-kHz ADCP (which is not used for an estimation of a wind-driven flow) and the drift

Table 1. Comparisons Between 300 kHz ADCP Velocity at 10 m depth and 1200 kHz ADCP Velocity at 8 m depth[a]

	A	B, cm s^{-1}	COR	RMS, cm s^{-1}	NUM
Zonal	1.14	−1.03	0.95	1.52	312
Meridional	0.97	1.43	0.97	1.43	312

[a]A and B are slope and intercept of regression line $v^{1200\ \mathrm{kHz}} = Av^{300\ \mathrm{kHz}} + B$, COR is correlation, RMS is root mean square distance from regression line, and NUM is number of samples. Regression line is obtained from PCA.

velocity estimated from hourly GPS data of the buoy can be used to estimate ADCP measurement error. RMS difference between the two velocities is 2.28 cm s^{-1}. Note that RMS difference is larger (3.12 cm s^{-1}) in the strong wind period (8–12 July, average wind magnitude was 6.13 m s^{-1}) and smaller (1.18 cm s^{-1}) in the weak wind period (14–18 July, average wind magnitude was 2.49 m s^{-1}). This suggests that wind and surface waves induce large platform motions to increase ADCP measurement error. The largest variance error of ADCP velocity is thus considered as a few centimeters per second.

3.2. Variance Error of HF Radar Velocity

[16] Measurement error of HF radar at the mooring site is examined by comparing HF radar radial velocity with a radial component of ADCP velocity at 3 m depth (Table 2). Comparisons show very good correlation with C2, N1, and N2 radar velocities. However, large unreasonable variance errors are found in C1 and C3 radar velocities. For this reason, only N1 and N2 (NJRC) radars are used in this study. The RMS difference from the regression line between ADCP and HF radar velocities is less than 3.08 cm s^{-1}. Since the variance error of ADCP is partly included in this RMS difference, this can be regarded as a maximum value of a possible variance error of HF radar radial velocity. A variance error of velocity vector magnitude is then calculated from a variance error of radial velocity as [*Nadai et al.*, 1999]

$$\sigma_v = \sqrt{\frac{2\sigma_r^2}{\sin^2(\theta_1 - \theta_2)}},$$

where σ_v is a variance error of vector magnitude, σ_r is a variance error of radial velocity, and $\theta_1 - \theta_2$ (=30°) is a difference between looking directions from the mooring site to N1 and N2 sites. A variance error of the vector magnitude is then estimated to be 8.85 cm s^{-1}.

3.3. Bias Errors of ADCP and HF Radar Velocities

[17] Bias error between HF radar and ADCP velocities can be estimated from regression coefficients obtained from ADCP and HF radar comparison. Slopes of the regression lines (1.01 and 0.88) are good, and intercepts (5.39 and 3.87 cm s^{-1}) seem reasonable if compared with variance errors of ADCP and HF radar. It should be noted that these regression coefficients reflect not only measurement errors but also a real difference due to different measurement depths, different averaging area, and orbital velocity aliased into ADCP velocity. Thus regression coefficients are considered to represent maximum values of possible bias errors of ADCP and HF radar. *Yoshikawa et al.* [2006] investigated variance and bias errors of HF radar in the Tsushima Strait to find that a variance error dominates over a measurement error of HF radar. Mean difference between the bottom-track velocity measured by the 300-kHz ADCP and the drift velocity estimated from hourly GPS data of the buoy is also small (0.89 cm s^{-1}). Thus we consider that bias errors of ADCP and HF radar velocities are reasonably small.

Table 2. Comparisons Between ADCP-Measured Velocity (at 3 m depth) and HF Radar-Measured Velocity[a]

Radar	DIS, km	A	B, cm s^{-1}	COR	RMS, cm s^{-1}	NUM
C1	73	0.49	7.27	0.66	4.30	287
C2	37	0.70	−0.95	0.87	2.68	331
C3	42	0.49	−1.27	0.39	5.95	326
N1	37	1.01	5.39	0.91	3.08	349
N2	52	0.88	3.87	0.90	3.01	342

[a]DIS is distance between radar site and mooring site. A, B, COR, RMS, and NUM are same as in Table 1 ($v^{\mathrm{radar}} = Av^{\mathrm{ADCP}} + B$).

Table 3. Comparisons Between JMA Wind Stress and the Tower Wind Stress[a]

	A	B, Pa	COR	RMS, Pa	NUM
zonal stress	0.92	3.59×10^{-3}	0.77	1.07×10^{-2}	90
meridional stress	1.28	4.32×10^{-3}	0.79	1.69×10^{-2}	90

[a]A, B, COR, RMS, and NUM are same as in Table 1 ($\tau^{\mathrm{tower}} = A\tau^{\mathrm{JMA}} + B$).

3.4. Wind Stress Error

[18] To examine whether the wind stress estimated from JMA-reanalyzed wind (referred to as JMA wind stress) is appropriate for the present analysis, wind data measured at marine tower station near the mooring site (Figure 1) operated till 2002 are used. Anemometer at the tower was attached above about 17 m from the sea surface and measured wind for 12 min every hour. The hourly wind is converted to hourly wind stress using drag coefficient formula of *Yelland and Taylor* [1996], and a low-pass filter (25 hours running mean) is applied to obtain smoothed hourly wind stress.

[19] The smoothed tower wind stress and JMA wind stress at the tower station are compared (Table 3) from 28 July to 27 August 2002 (in which no typhoon hit the tower). Though meridional component of JMA wind stress might underestimate that of the tower wind stress by a few 10%, we consider that agreement between two wind stress is relatively good and that JMA wind stress well represents local wind stress at our mooring site during the field observation.

4. Wind, Current, Water Temperature, and Orbital Velocity

[20] Figure 5 shows hourly wind and current velocities (every 6 hours). Wind is generally weak (3.94 m s^{-1} on average) except in 8–12 July when southerly wind often exceeds 10 m s^{-1} in magnitude. Current generally directs to the northeast due to the Tsushima Warm Current. Power spectra of wind stress and hourly current velocities (not shown) show that major part of wind and current energy lies at lower frequencies than the diurnal frequency.

[21] Figure 6 shows three typical power spectra of wave height ($P(f)$) measured at Fukuejima as a function of frequency (f). The spectra show large amplitude of both

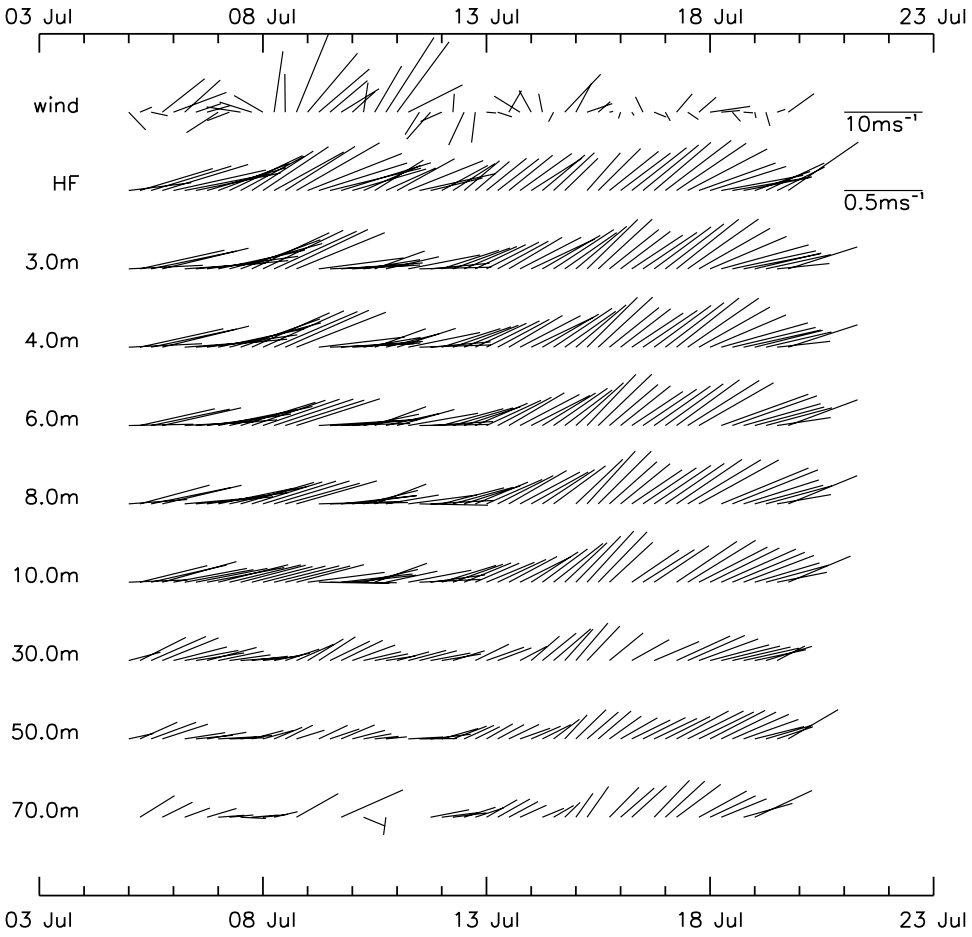

Figure 5. Hourly wind and current velocities during our field observation. Sampling interval is 6 hours.

long swell and short wind wave when wind is strong (9 July), small amplitude of both long swell and short wind wave when wind is weak (16 July), and large amplitude of only long swell when wind is weak (21 July). Thus wave of 10 s period is composed mostly of long swell, wave of 5 s period is composed of both long swell and locally generated short wind wave, and wave of 2.5 s period is composed mostly of short wind wave.

[22] Using linear theory, magnitude of total orbital velocity $v^{\mathrm{orb}}(f-\Delta f/2: f+\Delta f/2)$ of the waves in $(f-\Delta f/2, f+\Delta f/2)$ frequency range at z m depth can be estimated from power spectrum $P(f)$ as

$$v^{\mathrm{orb}}(f-\Delta f/2 : f+\Delta f/2) = 2\pi f\sqrt{P(f)\Delta f}\exp(-kz),$$

where $k(=(2\pi f)^2/g)$ is wave number. Here Δf of 2^{-5} s^{-1} is used. Magnitude of an aliasing velocity from the wave outside this frequency range is less than 0.5% of its original orbital velocity.

[23] Time series of the estimated orbital velocity magnitudes of 10, 5, and 2.5 s periods are shown in Figure 7. The velocity of 2.5 s period is quite small due to small energy and short vertical length scale. The velocity of 5 s period is about 7 cm s^{-1} for 8–12 July when wind is strong and otherwise less than a few centimeters per second. The velocity of long swell (10 s period) is about 5 cm s^{-1} for 8–12 July and after 20 July.

[24] Note that the above orbital velocities are all aliased into hourly ADCP velocity only if direction of wave propagation is unique and constant during 1 hour. Because

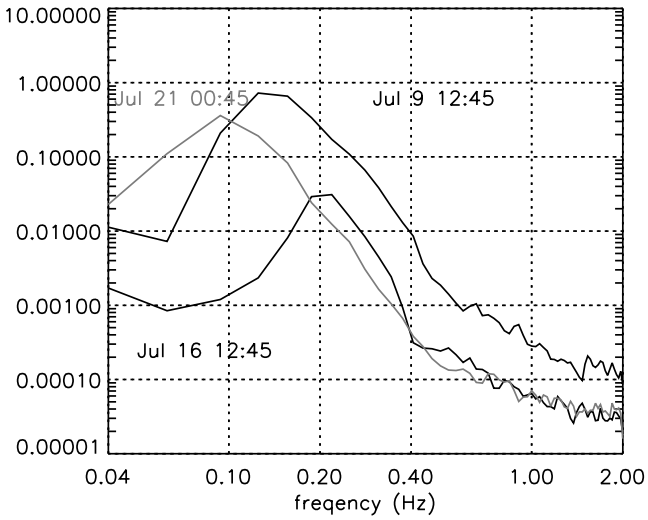

Figure 6. Power spectrum of wave height measured at Fukuejima station (JMA).

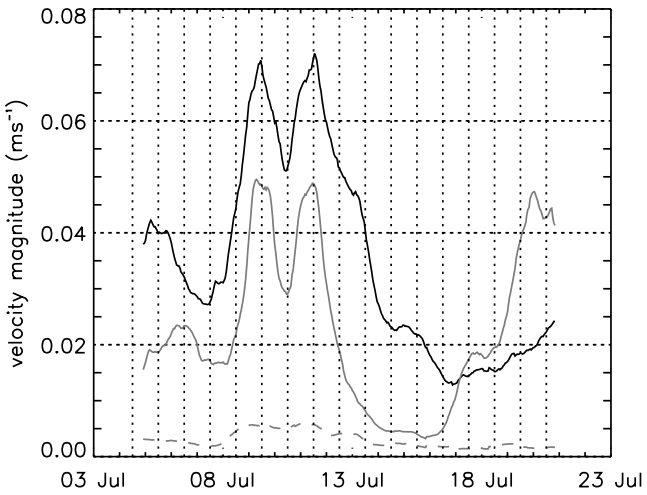

Figure 7. Orbital velocity magnitude $v^{\mathrm{orb}}(f - \Delta f/2 : f + \Delta f/2)$ at 3 m depth estimated from wave height spectrum using linear short-wave theory. The velocity represents total orbital velocity of the waves in $(f - \Delta f/2, f + \Delta f/2)$ frequency range ($\Delta f = 2^{-5}$ s^{-1}). Black line: velocity of 5 s wave period (both long swell and short wave). Gray line: velocity of 10 s wave period (long swell). Gray dashed line: velocity of 2.5 s period (short wave).

actual direction is neither unique nor constant, the velocity magnitude that is aliased into ADCP velocity would be smaller than 10 cm s^{-1}. In this study, a maximum value of a possible aliasing velocity is considered to be 10 cm s^{-1}.

[25] Figure 8 shows water temperatures measured by upper three thermometers. Temperatures increase gradually during our observation period. Diurnal variation of temperature is evident, but diurnal variation of thermal stratification is not clearly found. In particular, thermal stratification is negligible on 9–16 July. This is due probably to strong vertical mixing by the intense wind on 8–12 July.

5. Wind-Driven Velocity Structure

5.1. Relative Velocity

[26] To extract a wind-driven velocity from the observed (total) velocity, the velocity of an interior flow (referred to as a reference flow) is subtracted from a total velocity. The reference flow in the surface boundary layer is estimated from velocities at greater depths where a wind-driven flow is assumed to be negligibly small. The present analysis depends largely on the estimation of the reference flow. Sensitivities of the estimation on the present analysis will be described in later subsection, and the result with the most appropriate reference flow is presented in this subsection.

[27] The reference flow here is assumed to be linearly sheared and is estimated by extrapolating a velocity at 18 m depth to shallower depths with vertical shear averaged over 18- to 58-m-depth range. Subtraction of this reference velocity from a total velocity is expected to yield the velocity representing a wind-driven flow (referred to as a relative velocity or flow).

[28] Figure 9 shows hourly wind stress and the relative velocity (every 6 hours). The relative velocity is found to rotate clockwise with depth particularly in the period of strong wind stress (8–12 July). However, the relative velocity is large even in a weak wind stress period (before 7 July and after 13 July). This indicates that components other than the wind-driven flow covarying with wind stress, such as orbital velocity due to surface waves (particularly long swell), the flow triggered by wind stress but neither balanced with wind stress nor dissipated, and a baroclinic interior current with higher order vertical shear, are included in the relative velocity defined above. Although these components are expected to reduce in magnitude by long-time averaging [*Schudlich and Price*, 1998], record length of velocity data is too short in this study.

5.2. Complex Principal Component Analysis

[29] To extract the wind-driven flow covarying with time-varying wind stress from the relative flow defined above, we perform complex PCA [or empirical orthogonal function analysis; *Kundu and Allen*, 1976] of both the wind stress and the relative velocity during the whole observation period. Explained variance and a corresponding set of vectors (the wind stress and the relative velocity written in the complex form) of the first mode are obtained as the largest eigenvalue and the corresponding eigenvector of (complex) covariance matrix $\mathbf{C} = \mathbf{W}^{*T}\mathbf{W}$, respectively, where $\mathbf{W} = (\mathbf{w}_1, \mathbf{w}_2, \ldots, \mathbf{w}_K)$ and $\mathbf{w}_k$ ($k = 1, \ldots, K$) is an N-element row vector (N is the number of sampling time) of wind stress ($k = 1$) and relative velocities ($2 \leq k \leq K$). Conjugate transpose matrix of W is represented by $\mathbf{W}^{*T}$.

[30] Two normalizations are applied to $\mathbf{w}_k$. First, wind stress and the relative velocity are normalized by root mean squares of wind stress and the shallowest relative velocity (measured by HF radar), respectively. Second, wind stress is multiplied by $(K - 1)$, the number of levels of the relative velocities. By this normalization, the first mode is forced to mainly explain wind stress variance. The relative velocities of the first mode thus represent the velocity component covarying with wind stress. The second normalization enables the extraction of only the velocity component of

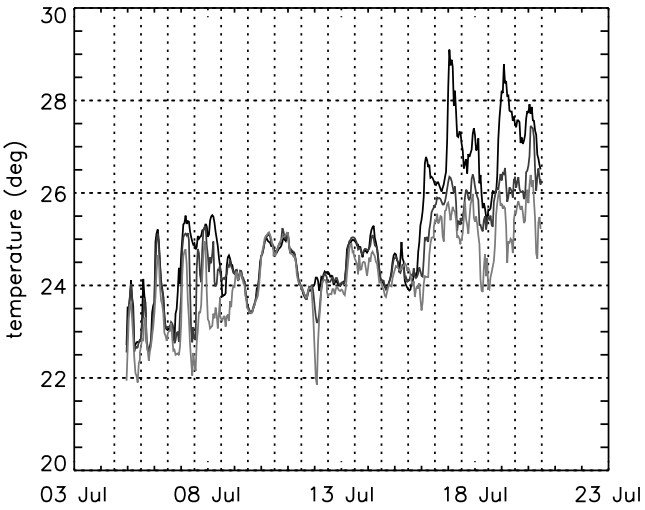

Figure 8. Time series of water temperatures at the sea surface (black line) and at 5 m (dark gray line) and 10 m (light gray line) distant from the surface along a mooring rope.

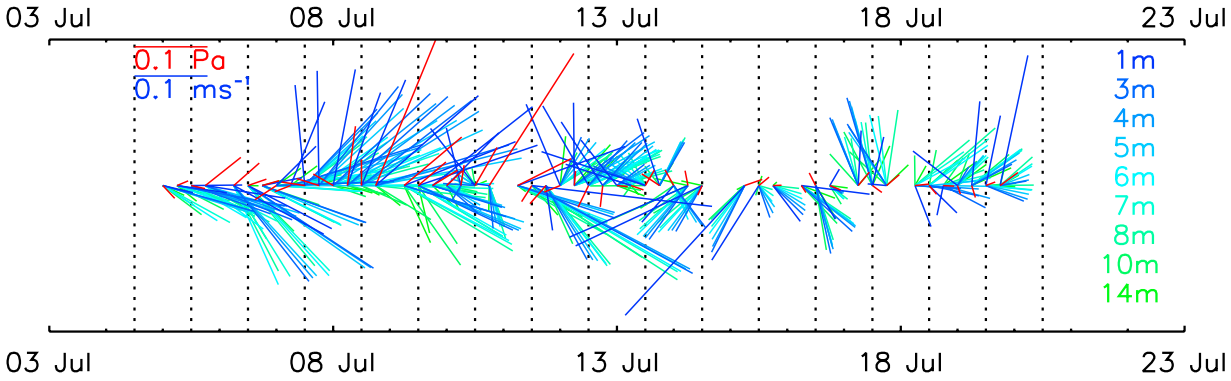

Figure 9. Hourly wind stress (red) and hourly relative velocities (blue to green). Color legends for the relative velocities are shown in the figure. Data are plotted only when both wind stress (obtained every 6 hours) and relative velocities are obtained.

relative velocity covarying with wind stress from total relative velocity.

[31] Normalized vector $\mathbf{w}_k$ is thus written as

$$\mathbf{w}_1 = \frac{K-1}{\mathrm{RMS}(\tau_x^{n'}, \tau_y^{n'})} \begin{pmatrix} \tau_x^{1'} + i\tau_y^{1'} \\ \tau_x^{2'} + i\tau_y^{2'} \\ \vdots \end{pmatrix},$$

$$\mathbf{w}_2 = \frac{1}{\mathrm{RMS}(u_{0.5\,\mathrm{m}}^{n}, v_{0.5\,\mathrm{m}}^{n})} \begin{pmatrix} u_{0.5\,\mathrm{m}}^{1} + iv_{0.5\,\mathrm{m}}^{1} \\ u_{0.5\,\mathrm{m}}^{2} + iv_{0.5\,\mathrm{m}}^{2} \\ \vdots \end{pmatrix},$$

$$\vdots$$

$$\left(\mathrm{RMS}(x^n, y^n) = \sqrt{\left(\Sigma_{n=1}^{N} x^{n2} + y^{n2}\right)/N}\right)$$

where i is the imaginary unit, ($\tau_x^{n'}$, $\tau_y^{n'}$,) is the hourly wind stress at $n' = n - h$ hour, h is the time lag between wind and current, and ($u_{z\ \mathrm{m}}^{n}$,$v_{z\ \mathrm{m}}^{n}$) is the hourly relative velocity measured at z m at n hour by HF radar ($z = 0.5$ m) or ADCP ($z \geq 3$ m). An adjustment of a wind-driven flow to wind stress is expected to take time, so that time lag (h) is introduced in this analysis. Note that wind stress is available only every 6 hours, so the hourly relative velocity is used when (lagged) wind stress is available.

5.3. The First Mode

[32] Two parameters, the reference flow and a time lag between the wind stress and the relative flow, must be specified before performing PCA. The reference velocity used in this subsection is the same as in the previous subsection, and the time lag is set to 11 hours since these parameters provide the most appropriate estimation of Ekman transport as described later.

[33] Figure 10 shows the velocity structure of the first mode. This mode explains 95.8% of the normalized variance. A high proportion of the first mode is due to the second normalization; the first mode is forced to explain wind stress variance to which much weight is given.

[34] The first mode seems to represent an Ekman spiral balanced to the local wind stress at 11 hours ago. Figure 11 shows vertical profiles of velocity magnitude and direction of the first mode and those of an Ekman solution obtained with uniform eddy viscosity of 5.0×10^{-3} m^2 s^{-1}. A velocity profile of the first mode is less smooth than the theoretical one. A velocity magnitude of the first mode is smaller than that of theoretical one near the surface due probably to large eddy viscosity near the surface (section 6). On the other hand, a velocity of the first mode rotates as much as the theoretical one. This is in contrast to previous studies in which a velocity spiral is flatter than Ekman theory. *Price et al.* [1986] showed the importance of diurnal

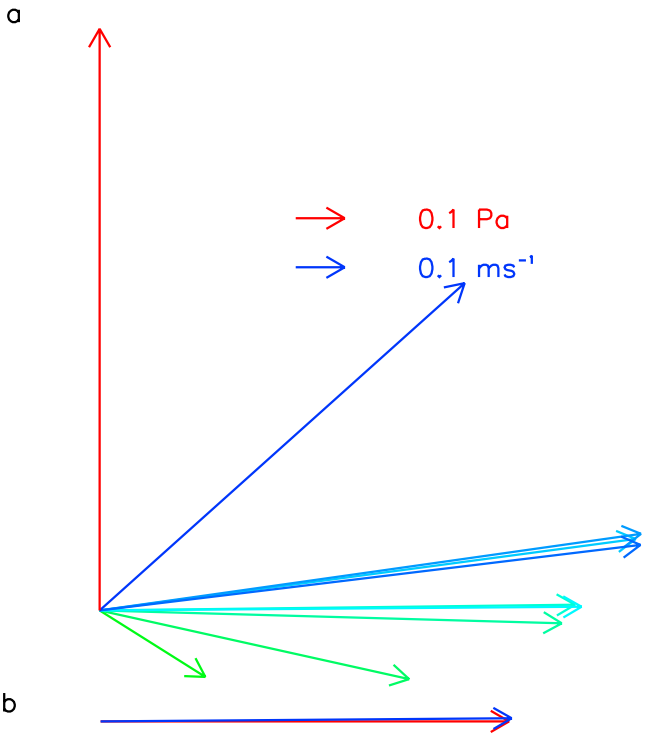

Figure 10. (a) Wind stress and relative velocities of the first mode. Color legends are same as in Figure 9. (b) Ekman transport estimated from integration of the relative velocities of the first mode (blue) and Ekman transport expected from the wind stress of the first mode (red). Wind stress is set to point to the north.

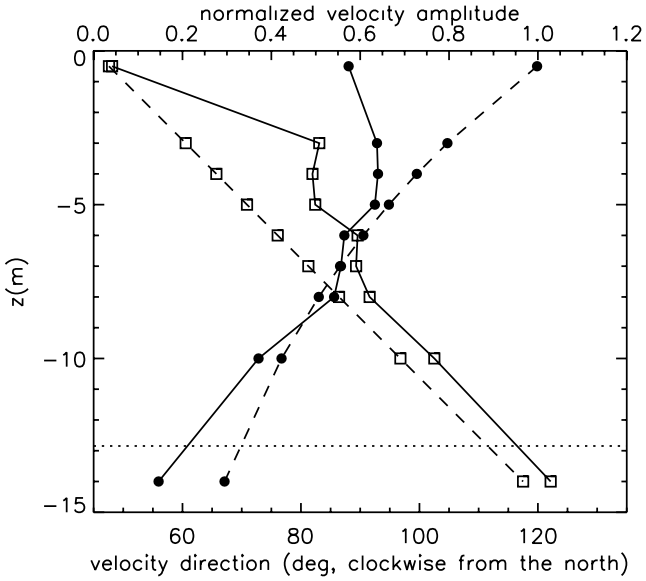

Figure 11. Vertical profile of velocity magnitude (solid circle) and direction (open square) of the first mode (solid line) and an Ekman solution (dashed line) calculated with vertical eddy viscosity of 5×10^{-3} m^2 s^{-1}. Dotted line represents *e*-folding depth scale calculated from magnitude of the relative velocities. Wind stress is set to point to the north.

cycle of stratification on flat spiral formation. In our observation period, stratification is negligibly small during strong wind (Figure 8). This is the most probable cause of less flat spiral in this study. Velocity magnitude and direction at 3–5 and 6–8 m group together, respectively, as if there are slab sublayers of 3 m thickness at these depths.

[35] Figure 10 also shows the Ekman transport estimated from integration of the relative velocities of the first mode (referred to as the estimated Ekman transport) and the transport expected from the wind stress of the first mode (referred to as the expected Ekman transport). Very good agreement between two transports suggests Ekman balance between the wind stress and the relative velocities of the first mode.

[36] Figure 12 shows time series of the (lagged) wind stress and the relative velocities (upper panel), those of the first mode (middle panel), and those of the higher modes (lower panel). It is clear that the velocity component covarying with wind stress is successfully extracted from the total relative velocity (upper panel) as the first mode (middle panel). The first mode, however, explains only 28.9% of the "current" velocity variance ($\Sigma_{k=2}^{K}|\mathbf{w}_k|^2$). This is because much weight is attached to wind stress, and hence the first mode is selected to explain first the wind stress variance. This also indicates that velocity component not covarying with wind stress dominates the relative velocity variance. Sources of this component are discussed in section 6.

5.4. Sensitivity to Reference Flow

[37] The simplest definition of the reference flow is to assume a vertically uniform (barotropic) interior flow as in the previous studies. In this definition, a reference depth (whose velocity is set to a velocity of the uniform reference flow) is only parameter to be specified. Table 4 shows the estimated and the expected Ekman transport for several reference depths. The most appropriate reference depth is found to be 18 m although there remains difference in direction between two transports.

[38] A second simple definition of the reference flow is to assume a linearly sheared interior flow. In this definition, not only the reference depth but also (uniform) the vertical shear of the reference flow (referred to as a reference shear) must be specified to extrapolate a velocity at the reference depth. Although there are many possible definitions of the reference shear, the most appropriate one will be the shear averaged over a certain depth range just below the reference depth. In this case, the parameters to be examined are the reference depth and the depth range over which averaged shear is estimated.

[39] Several reference depths and average depth ranges are examined (Table 4). It is found that very good agreement between the estimated and the expected Ekman transport is obtained for the reference depth of 18 m and the average depth range of 40 m.

5.5. Sensitivity to Time Lag

[40] Figure 13 shows the ratio of explained variance to total variance (score) of the first mode, the ratio of explained "current" variance to total "current" variance of the first and second modes, the magnitude ratio of the estimated Ekman transport to the expected one, and the direction difference between the estimated and the expected Ekman transport as a function of time lag. The 95% confidence intervals estimated from variance errors of ADCP and HF radar velocity (Appendix) are also shown in Figure 13. Here variance error of HF radar velocity is set to 8.85 cm s^{-1} (section 3) and that of ADCP velocity is set to 10 cm s^{-1}, taking into account the possible aliasing of orbital velocity due to surface waves (section 4).

[41] In this subsection, the linearly sheared reference flow with the reference depth of 18 m and the average depth range for the reference shear of 40 m is assumed. Ratio of explained variance of the first mode is 94.9% without time lag and increases gradually to be largest (95.6–95.8%) for 10- to 17-hour time lags. Ratio of explained "current" variance of the first mode also shows similar change with time lag and is largest (28.4–29.6%) for 11- to 13-hour time lags, for which ratio of explained "current" variance of the second mode is smallest (60.7–62.1%). A magnitude of the estimated Ekman transport is closest (within a 2.06% difference) to that of the expected Ekman transport for 11- to 13-hour time lags. Direction difference between the transports is also smallest (0.44°–3.08°) for these time lags. All these results suggest that the wind-driven flow is balanced with a wind stress after 11–13 hours, which corresponds to half of the inertial period (21.5 hours).

[42] Note that wind stress error and possible bias errors of ADCP and HF radar velocities are not considered in the present analysis. In particular, the orbital velocity due to short wind waves, which will covary with wind stress, might be aliased into hourly ADCP velocity of the first mode, although the aliased velocity will be much less than 7 cm s^{-1} (Figure 7), which is estimated as the largest velocity under the assumption of a unique and constant direction of wave propagation (section 4). Taking into account this possible errors and aliasing velocity, it should be considered

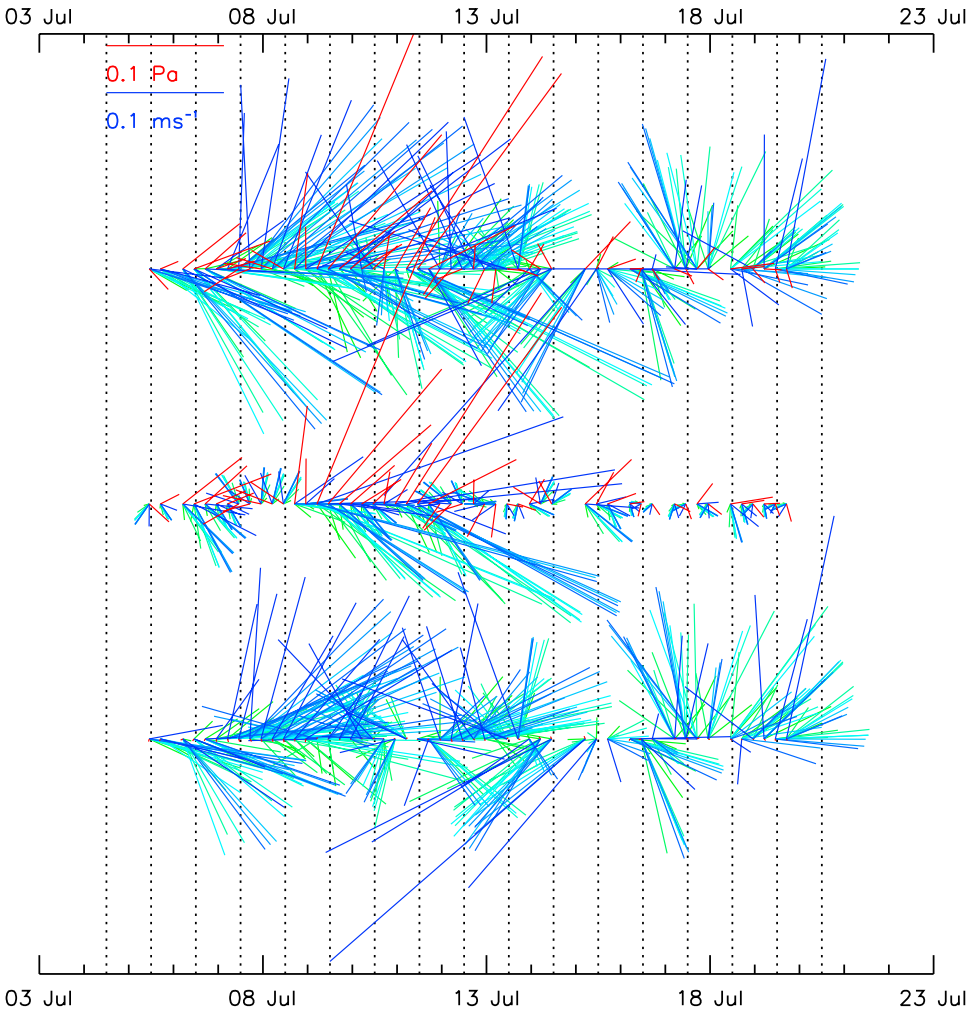

Figure 12. Time series of wind stress and relative velocities. Upper: total wind stress and relative velocities. Middle: wind stress and relative velocities of the first mode. Lower: wind stress and relative velocities of higher modes than the first. Color legends are same as in Figure 9.

that the discrepancy in the Ekman transports for the more traditional approach (vertical uniform reference flow and zero time lag) is also small.

6. Discussion

6.1. The Second Mode

[43] The major part of the velocity components not covarying with wind stress is represented by the second mode. It explains only 3.68% of total normalized variance ($\Sigma_{k=1}^{K}|\mathbf{w}_k|^2$) but 62.1% of "current" variance ($\Sigma_{k=2}^{K}|\mathbf{w}_k|^2$). Possible sources of the second mode are discussed in this subsection.

[44] Figure 14 shows the velocity structure of the second mode. Noteworthy is that the second mode shows clockwise velocity spiral with depth. This suggests that the second mode represents the mismatch between the actual wind stress and the JMA wind stress estimated from reanalyzed wind and drag coefficient formula. However,

Table 4. Comparisons Between the Estimated and the Expected Ekman Transport[a]

	U		S									
			D = 24 m		D = 32 m		D = 40 m		D = 48 m		D = 56 m	
z_r, m	r	$\Delta\theta$, °	r	$\Delta\theta$, °	r	$\Delta\theta$, °	r	$\Delta\theta$, °	r	$\Delta\theta$, °	r	$\Delta\theta$, °
10	0.42	42.5				0.29	41.8					
14	0.88	25.8				0.70	15.2					
18	1.18	16.5	0.89	−3.4	0.97	−1.4	1.01	0.4	1.00	3.0	1.01	5.2
22	1.50	18.4				1.27	1.7					
26	1.89	24.6				1.54	9.5					

[a]U indicates a uniform reference flow, and S indicates a linearly sheared reference flow. z_r is the reference depth, D is the averaging depth (the reference shear is estimated from average velocity shear between z_r and $z_r + D$), r is the magnitude ratio of the estimated to the expected Ekman transport, and $\Delta\theta$ is the direction difference between the estimated and the expected Ekman transport. Time lag of 11 hours is assumed.

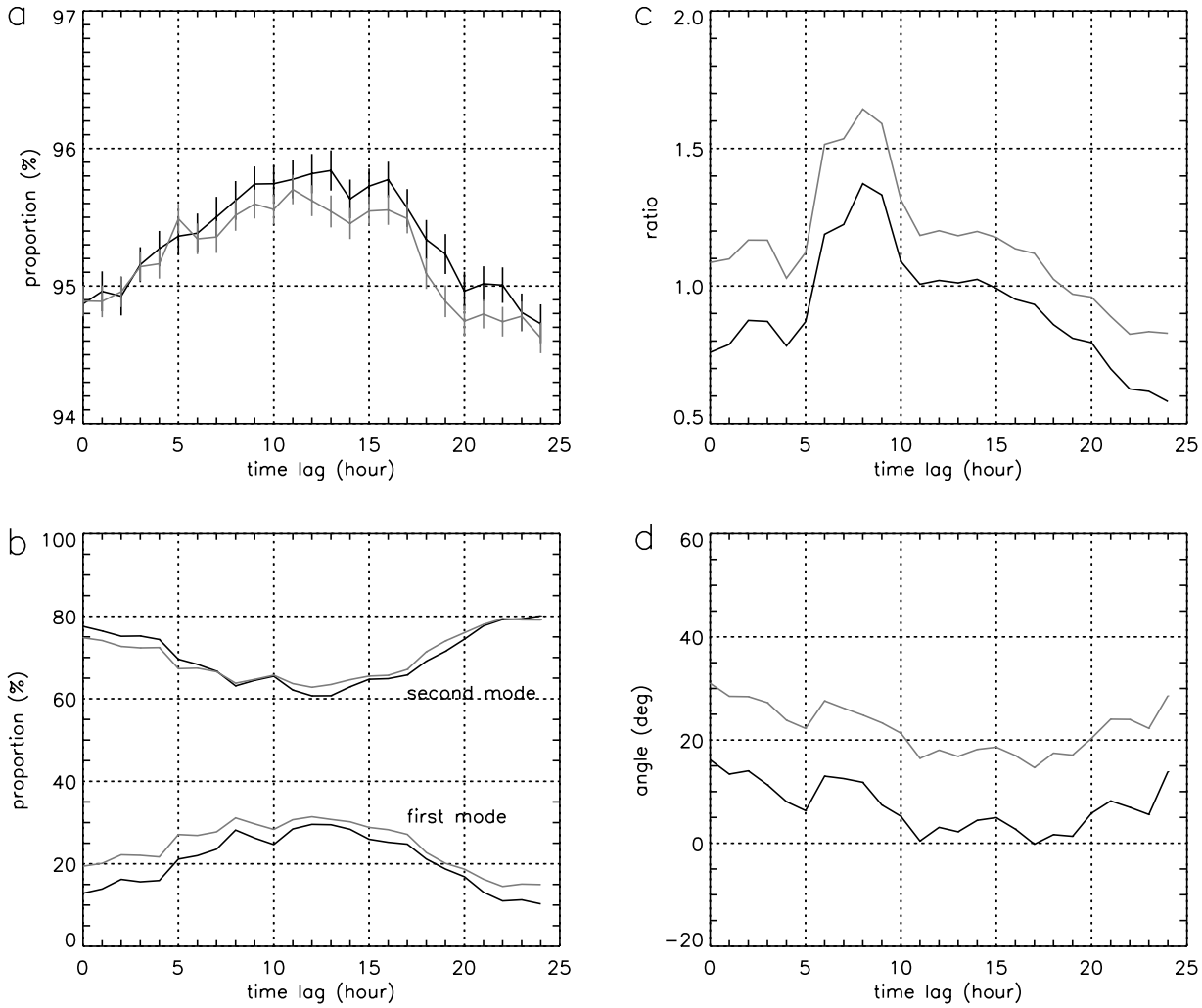

Figure 13. Explained variance and Ekman transport as a function of time lag. (a) Ratio of explained variance of the first mode. (b) Ratio of explained "current" variance of the first and second modes. (c) Magnitude ratio of the estimated Ekman transport to the expected Ekman transport. (d) Direction difference between the estimated and the expected Ekman transport. Black line indicates a linearly sheared reference velocity, and gray line represents a vertically uniform reference velocity. The 95% confidence interval is represented by vertical bar in Figure 13a but not in Figures 13b, 13c, and 13d due to its small value. Largest confidence intervals are (a) 0.29%, (b) 0.02%, (c) 4.5×10^{-4}, and (d) 2.0×10^{-4}.

our estimation of JMA wind stress error (section 3) is less than a few 10%. This is not large enough to explain twice larger current variance of the second mode than that of the first mode.

[45] Figure 15 shows a time series of magnitude of the second mode score, an intensity of the components of relative velocity not covarying with wind stress. Subinertial oscillation is evident in the time series. This indicates that a wind-driven flow that is triggered by wind stress, but is not balanced with wind stress at 11 hours ago, is also partly responsible for the second mode. It should also be noted that the higher mode velocities (lower panel of Figure 12) do not always show clockwise spiral (for example, from 16 to 21 July), suggesting a possible effect of higher-order velocity shear of interior flow. Intensity of the higher-order velocity shear can be estimated from γ_u and γ_v defined by

$$\gamma_u = \left| \frac{\Gamma_u(z_r + D/2 : z_r + D)}{\Gamma_u(z_r : z_r + D)} - 1 \right|,$$

$$\gamma_v = \left| \frac{\Gamma_v(z_r + D/2 : z_r + D)}{\Gamma_v(z_r : z_r + D)} - 1 \right|,$$

where $\Gamma_u(z_1 : z_2) = (u(z_1) - u(z_2))/(z_2 - z_1)$ and $\Gamma_v(z_1 : z_2)$ $(v(z_1)$ $(v(z_1) - v(z_2))/(z_2 - z_1)$ represent averaged velocity shear of zonal and meridional components over $z_1 \leq z \leq z_2$, respectively. Note that $\gamma_u = \gamma_v = 0$ if shear of an interior

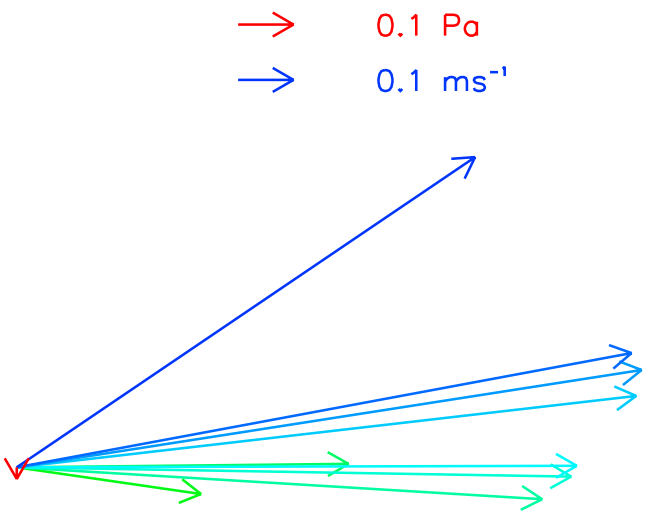

Figure 14. Wind stress and relative velocities of the second mode. Color legends are same as in Figure 9. Wind stress is set to point to the south.

flow is vertically uniform, and it becomes larger if higher-order velocity shear becomes larger. Time series of $(\gamma_u + \gamma_v)/2$ is also plotted in Figure 15. It corresponds roughly to time series of the second mode score. This indicates that higher-order velocity shear of an interior flow is also a source of the second mode.

[46] As well as the above sources, orbital velocity associated with surface waves (particularly long swell) might be responsible for the second mode. The second mode is thus expected to be composed of several sources described above.

6.2. Eddy Viscosity

[47] Good agreement between the estimated and the expected Ekman transport found in the previous section suggests Ekman balance between the wind stress and the relative velocities of the first mode. This allows us to infer vertical eddy viscosity ($\mu(z)$) from turbulent Reynolds stress ($\tau_x(z)$, $\tau_y(z)$) and the relative velocities ($u(z)$, $v(z)$) of the first mode using the following two equations [e.g., *Chereskin*, 1995]:

$$if(u(z) + iv(z)) = \frac{\partial}{\partial z}\frac{\tau_x(z) + i\tau_y(z)}{\rho},$$

$$\frac{\tau_x(z) + i\tau_y(z)}{\rho} = \mu(z)\frac{\partial}{\partial z}(u(z) + iv(z)),$$

where ρ (=1020 kg m^{-3}) is water density. Three-point smoothing in the vertical is first applied to $u(z)$ and $v(z)$, and the first equation is integrated from the surface (where turbulent stress is assumed equal to wind stress) to greater depth to give $\tau_x(z)$ and $\tau_y(z)$. Vertical eddy viscosity is then diagnosed from the second equation. Although eddy viscosity estimated in this way can be a complex number, only its real part has a physical meaning. The imaginary part can be interpreted as a measure of the invalidity of Ekman balance.

[48] Figure 16 shows vertical profiles of turbulent stress and eddy viscosity. Turbulent stress is largest at the surface and smoothly reduces in magnitude at greater depth as expected from Ekman theory. The real part of eddy viscosity is also largest (1.2×10^{-2} m^2 s^{-1}) near the surface and becomes smaller (7.3×10^{-4} m^2 s^{-1}) at greater depth. A profile of eddy viscosity is less smooth than that of turbulent stress since the former is calculated from a derivative of the relative velocity (and hence is likely to be contaminated by noise) while the latter is estimated from its integration. Magnitude of eddy viscosity corresponds to Ekman depth $(2\mu/f)^{1/2}$ of 4.24–17.2 m, in which an e-folding depth scale (12.8 m) of the relative velocities of the first mode lies (Figure 11).

[49] Inferred eddy viscosity increases with height up to 2.5 m depth where wave motion is dominant. *Chereskin* [1995] also inferred eddy viscosity deeper than 8 m depth from observed velocity spiral to find that eddy viscosity is generally larger at shallower depths. These results do not agree with the eddy viscosity model proposed by *Madsen* [1977], in which logarithmic boundary layer and decreasing eddy viscosity with height are assumed. The possible cause of increasing eddy viscosity with height will be wave-induced turbulence, which will be larger at shallower depths, although it cannot be confirmed in the present study.

[50] A large imaginary part of eddy viscosity on the other hand suggests invalidity of the above estimation. There will be several reasons for this invalidity. One is bias errors of ADCP and HF radar velocities. Use of different devices that have different measurement properties might affect the anomalously small estimation of eddy viscosity at 3.5 m depth. Second is an assumption of constant eddy viscosity. Actual eddy viscosity is large when wind is strong, as expected from time variation of thermal stratification (Figure 8). Thus, for further discussion of eddy viscosity profile, it needs to be measured in a quantitative manner by, for example, a microstructure profiler.

7. Concluding Remarks

[51] Moored ADCP velocities and HF radar velocities for 2 weeks are investigated to detect a velocity structure

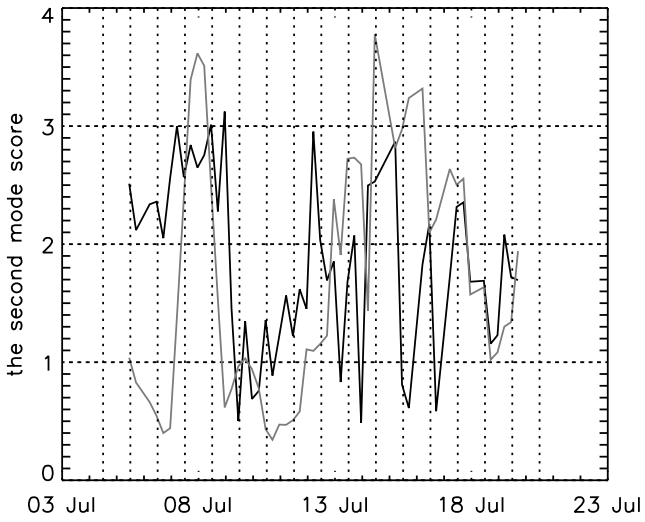

Figure 15. Magnitude of the second mode score (black line). Gray line shows an intensity of higher-order velocity shear of an interior flow ($(\gamma_u + \gamma_v)/2$).

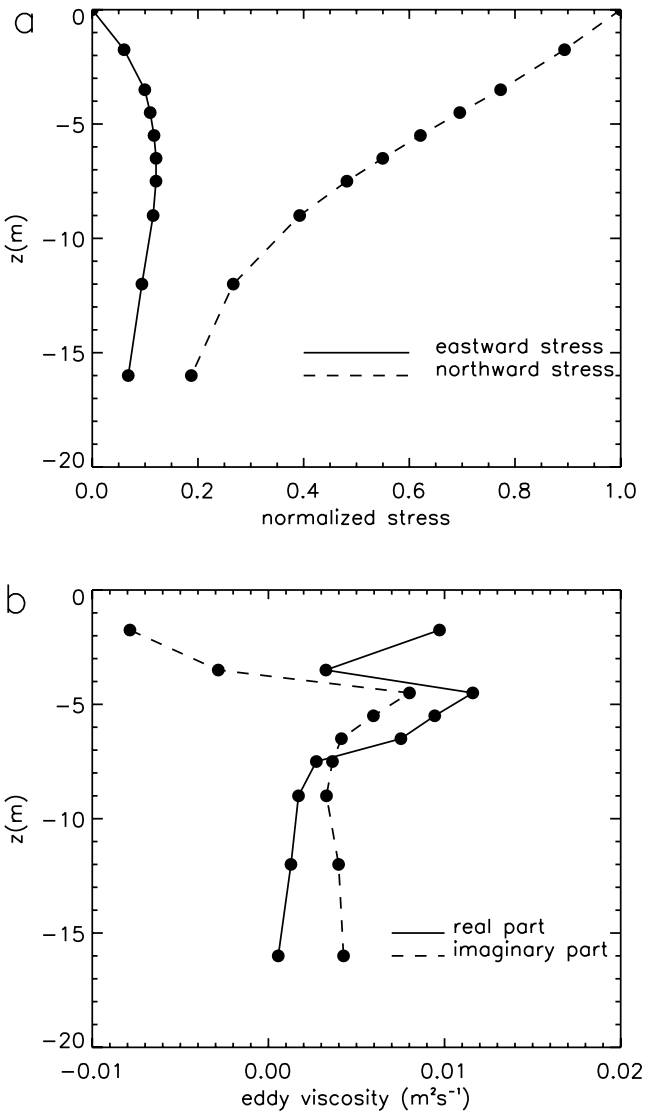

Figure 16. (a) Turbulent Reynolds stress and (b) eddy viscosity inferred from wind stress and relative velocities of the first mode shown in Figure 10.

(spiral) in the surface boundary (Ekman) layer in the Tsushima Strait. Simultaneous use of two ADCPs of high and low acoustic frequencies and HF radar enables velocity measurement in both the surface boundary layer and the interior with high resolutions. A velocity relative to an interior flow in the surface boundary layer is estimated by subtracting the reference velocity from a total velocity, and complex PCA of lagged wind stress and relative velocity is performed. Despite a short (2 weeks) observation period of relatively calm and variable wind, a clockwise velocity spiral similar to a theoretical Ekman spiral is detected as the first mode of PCA.

[52] Two types of the reference flow, a vertically uniform (barotropic) flow (as in previous studies) and a linearly sheared flow, are examined. For both types, the most appropriate reference depth is found to be 18 m. Agreement between Ekman transport estimated from the relative velocities and Ekman transport expected from wind stress is best for both magnitude and direction for a linearly sheared reference flow with time lag of 11–13 hours (half of the inertial period at this latitude).

[53] Once a wind-driven flow structure is known, an interior (subsurface) flow which transports a large body of water and materials can be estimated from HF radar measurement. The present study is a first step toward such a work. A velocity structure (spiral), however, will change seasonally according to a large seasonal variation in wind and stratification [e.g., *Schudlich and Price*, 1998]. Thus a velocity structure in other seasons needs to be examined. The present study also suggests that the velocity not covarying with wind stress is larger than the velocity covarying with wind stress. To estimate subsurface flow field from hourly HF radar measurement, quantitative estimates of the dominant source of the flow not covarying with wind and its structure are also required.

[54] It is also interesting that the depth of wind-driven flow (18 m) estimated in this study corresponds to a typical depth of surface low-salinity water in this strait (approximately 20 m). Whether these two depths are related or not will be understood by comparing seasonal variations of a velocity spiral and typical depth of the low-salinity water. The presence of the sublayer in which the wind-driven velocity is vertically uniform and an increasing eddy viscosity with height need to be validated by further velocity and microstructure (turbulence) measurements in the surface layer. These will be our future works.

Appendix A

[55] Confidence interval in Figure 13 is estimated as follows. Given that variance errors of ADCP velocity at each level and HF radar velocity are independent to each other, covariance matrix derived from measured velocity $\mathbf{C}$ is expressed by covariance matrix derived from true velocity $\mathbf{C}^{\text{true}}$ and variance error matrix $\mathbf{C}^{\text{error}} = \{c_{ij}^{\text{error}}\}$ as

$$\mathbf{C} = \mathbf{C}^{\text{true}} + \mathbf{C}^{\text{error}}$$

$$c_{ij}^{\text{error}} = \begin{cases} \sum_{n=1}^{N} \varepsilon_k^{n2} & for \quad i = j = k(\geq 2) \\ 0 & otherwise \end{cases}$$

where ε_k^n is a variance error of HF radar velocity ($k = 2$) and ADCP velocity ($3 \leq k \leq K$) at time n. Assuming that a variance error is represented by Gaussian function, $\mathbf{C}^{\text{error}}$ is estimated from chi-square distribution. Significant interval is obtained by performing PCA of $\mathbf{C} \pm \mathbf{C}^{\text{error}}$.

[56] **Acknowledgments.** We would like to express our gratitude to Joji Ishizaka and the captain, officers, and all crew members of T/V Nagasaki-Maru of Nagasaki University for their cooperation in deployment and recovering of a surface moored buoy. We also wish to thank James Richman, anonymous reviewers, and Akira Masuda for their instructive comments. Our field observation is supported by Tomoharu Senjyu, Tetsutaro Takikawa, the captain of T/V Wakasugi of Kyushu University, and the captain of T/V Tenyou-Maru of National Fisheries University. Chikara Shimoda of SEA Corporation suggests many technical pieces of advice associated with ADCP. Makoto Yasunaga, Masaru Inada, and Michiyoshi Ishibashi of Kyushu University help to accomplish our field observation. This study is a part of the project "Monitoring and prediction of marine and atmospheric environmental changes in the East Asia" in the

Research Institute for Applied Mechanics, Kyushu University. This study is also supported in part by Grant-in-Aid for Scientific Research (B) of the Ministry of Education, Culture, Sports, Science and Technology (17340141).

References

Chereskin, T. K. (1995), Direct evidence for an Ekman balance in the California Current, *J. Geophys. Res.*, *100*(C9), 18,261–18,269.

Ekman, V. W. (1905), On the influence of the Earth's rotation on ocean currents, *Ark. Mat. Astron. Fys.*, *2*, 1–53.

Kundu, P. K., and J. S. Allen (1976), Some three-dimensional characteristics of low-frequency current fluctuations near the Oregon coast, *J. Phys. Oceanogr.*, *6*, 181–199.

Lee, C. M., and C. C. Eriksen (1996), The subinertial momentum balance of the North Atlantic subtropical convergence zone, *J. Phys. Oceanogr.*, *26*, 1690–1704.

Madsen, O. S. (1977), A realistic model of the wind-induced Ekman boundary layer, *J. Phys. Oceanogr.*, *7*, 248–255.

Nadai, A., H. Kuroiwa, M. Mizutori, and S. Sakai (1999), Measurement of ocean surface currents by the CRL HF ocean surface radar of FMCW type: Part 2. Current vector, *J. Oceanogr. Soc. Jpn.*, *7*, 248–255.

Price, J. F., R. A. Weller, and R. Pinkel (1986), Diurnal cycling: Observations and models of the upper ocean response to diurnal heating, cooling, and wind mixing, *J. Geophys. Res.*, *91*(C7), 8411–8427.

Richman, J. G., R. A. DeSzoeke, and R. E. Davis (1987), Measurement of near-surface shear in the ocean, *J. Geophys. Res.*, *92*(C3), 2851–2858.

Schudlich, R. R., and J. F. Price (1998), Observation of seasonal variation in the Ekman layer, *J. Phys. Oceanogr.*, *28*, 1187–1204.

Stacey, M. W., S. Pond, and P. H. LeBlond (1986), A wind-forced Ekman spiral as a good statistical fit to low-frequency currents in a coastal strait, *Science*, *223*, 470–472.

Weller, R. A. (1981), Observations of the velocity response to wind forcing in the upper ocean, *J. Geophys. Res.*, *86*(C3), 1969–1977.

Weller, R. A., D. L. Rudnick, C. C. Eriksen, K. L. Polzin, N. S. Oakey, J. W. Toole, R. W. Schmitt, and R. T. Pollard (1991), Forced ocean response during the Frontal Air-Sea Interaction Experiment, *J. Geophys. Res.*, *96*(C5), 8611–8638.

Wijffels, S., E. Firing, and H. Bryden (1994), Direct observation of the Ekman balance at 10°N in the Pacific, *J. Phys. Oceanogr.*, *24*, 1666–1679.

Yelland, M., and P. K. Taylor (1996), Wind stress measurement from the open ocean, *J. Phys. Oceanogr.*, *26*, 541–558.

Yoshikawa, Y., A. Masuda, K. Marubayashi, M. Ishibashi, and A. Okuno (2006), On the accuracy of HF radar measurement in the Tsushima Strait, *J. Geophys. Res.*, *111*, C04009, doi:10.1029/2005JC003232.

K. Fukudome, Interdisciplinary Graduate School of Engineering Sciences, Kyushu University, Kasuga, Fukuoka, Japan.

K. Marubayashi, T. Matsuno, and Y. Yoshikawa, Research Institute for Applied Mechanics, Kyushu University, 6-1 Kasuga Park, Kasuga, Fukuoka 816-8580, Japan. (yosikawa@riam.kyushu-u.ac.jp)